APPROACH TO MAGNETIC ACTUATION OF A SOFT INSPECTION ROBOT FOR HVDC TRANSMISSION LINES

Xian Jin Xu,* Hai Feng Yan,* Lanlan Liu,** Yu Yan,** Yan Hao Huang,* and Yu Hang Yang*

Abstract

Currently, the existing high-voltage transmission line inspection robots used in both domestic and foreign research mostly adopt a multi-link rigid structure. However, such designs suffer low obstacle-surmounting efficiency and inadequate safety, making them difficult to be practical. In this paper, a high-voltage magnetostrictive soft inspection robot is designed, utilising the ampere force exerted on the current-carrying coil in a high-voltage direct current annular magnetic field to drive the soft robot to efficiently and flexibly traverse various obstacles in a creeping and compliant manner. The paper conducts theoretical analysis and magnetic field simulation to characterise the annular magnetic fields around different types of obstacles. The design and theoretical calculation of the magnetostrictive model for linear traction force, magnetic adhesion force (tensile force), and adjustment of posture torque are carried out to ensure the driving force theory feasibility. Additionally, force analysis is conducted to examine the motion postures required for crossing different types of obstacles. Simulation and dynamic analysis of the magnetostrictive model prove the theoretical feasibility of the proposed high-voltage magnetostrictive soft inspection robot scheme, laying a foundation for future technological implementation of high-voltage magnetostrictive soft inspection robots.

Key Words

High voltage DC transmission lines; soft robots; magnetic actuation; dynamics; magnetic field simulation

1. Introduction

The high-voltage inspection robot significantly ensures the stable operation of China's high-voltage direct current grid. Since the 1980s, extensive research has been conducted on high-voltage inspection robots both domestically and internationally. Examples include the "Expliner" inspection robot developed by Paulo Debenest and his team from HiBot in Japan [1], the "LineScout" inspection robot from the Hydro-Quebec Research Institute in Canada [2]–[4], and two autonomous inspection robots capable of travelling along single conductors and ground wires, successfully developed by Professor Wu Gongping from Wuhan University in China [5]–[7], among others. However, the current rigid cantilever inspection robots have certain limitations, such as complex structure, limited flexibility, high maintenance costs, and poor adaptability, which hinder their practicality. The traditional manual inspection method is no longer suitable for today's large-scale and high-intensity inspection tasks. Helicopter inspection methods are expensive, difficult to organise and implement, have inspection blind spots, and are subject to weather and aviation restrictions [8]. In recent years, unmanned aerial vehicles (UAVs) have gained popularity due to their safety, cost-effectiveness, and high efficiency. However, they still face challenges, including poor battery life and weather limitations, making it difficult to efficiently and effectively complete tasks [9]. In light of these challenges, this paper proposes a novel solution, the high-voltage magnetostrictive soft robot inspection system [10]–[13], which integrates different structures of soft robots with different coils. The circular magnetic field generated by the high-voltage lines surrounding the coils exerts an ampere force on the current-carrying coils, serving as the driving force for the soft robot. Leveraging the advantages of soft robots, such as redundancy in degrees of freedom, good continuity, and flexibility, the robot can flexibly cross suspension clamps and jumpers. Furthermore, it can also overcome obstacles, such as insulator discs and shock absorbers by crawling in an "Ω" shape.

This paper primarily introduces a new type of high-voltage magnetostrictive soft robot inspection system, which simulates the magnetic field around the four-split high-voltage lines and four types of obstacles and designs the robot's configuration. The driving mechanism of the robot is analysed, considering the pose and motion of the robot crossing the four different obstacles. Based on the magnetic field, the minimum driving force required for

* School of Mechanical Engineering, Hubei University of Technology, Wuhan, Hubei, China; e-mail: xxjoyjn@126.com; {624709248, 87356266}@qq.com; treeland3@163.com

** Hunan Province Key Laboratory of Intelligent Live Working Technology and Equipment (Robot), State Grid of Hunan Electric Power Company, Changsha, China; e-mail: 249841378@qq.com; 380147536@qq.com

Corresponding author: Hai Feng Yan and Lanlan Liu

(DOI: 10.2316/J.2024.206-1036)

the soft robot to traverse each obstacle is calculated and simulated. Furthermore, dynamic analysis and modelling of the most complex "Ω" crawling obstacle are conducted using the Lagrangian method [14]–[15].

2. Soft Robot Body Configuration

2.1 Magnetic Field Distribution of Overhead HVDC Transmission Lines

The high-voltage magnetostrictive soft robot inspection robots are designed to move along a single high-voltage line and utilise the ampere force generated by the current-carrying coil within the circular magnetic field around the high-voltage line as the driving force. The overhead high-voltage direct current transmission line consists of multiple split high-voltage conductors. Thus, in this paper, a four-split high-voltage line is considered as an example. The cross-section of the line is shown in Fig. 1, where the four high-voltage conductors carry currents in the same direction, perpendicular to the plane and pointing outward. Point O is selected on the circle with high-voltage line A as the centre, having a radius of d_0. The angles between the line segments connecting point O with high-voltage lines A, B, C, and D and the vertical direction are denoted as β, α, γ, and θ, respectively. A Cartesian coordinate system is established with point O as the centre, and B_a, B_b, B_c, and B_d represent the magnetic induction intensity of high-voltage lines A, B, C, and D at point O, respectively. The projections of B_a, B_b, B_c, and B_d on the X-axis and Y-axis are denoted as B_{ay}, B_{by}, B_{cy}, B_{dy}, B_{ax}, B_{bx}, B_{cx}, and B_{dx}. By applying the Biot-Savart theorem and considering the geometric relationships, the total magnetic field induction on the Y-axis can be determined as follows:

$$\begin{aligned} B_y &= B_{\mathrm{ay}} + B_{\mathrm{by}} + B_{\mathrm{cy}} + B_{\mathrm{dy}} \\ &= \frac{U_0 I}{2\pi}\left[\frac{\sin\beta}{L_{\mathrm{OA}}} + \frac{L_{\mathrm{OA}}\sin\beta}{L_{\mathrm{OB}}}\right. \\ &\quad + \frac{L - \sin\beta \cdot L_{\mathrm{OA}}}{L^2_{\mathrm{OA}} + L^2 - 2L_{\mathrm{OA}} \cdot L \cdot \sin\beta} \\ &\quad \left. + \frac{L - \sin\beta \cdot L_{\mathrm{OA}}}{L^2_{\mathrm{OA}} + 2L^2 - 2L_{\mathrm{OA}}(cos\beta + \sin\beta)}\right] \quad (1) \end{aligned}$$

The vacuum permeability is $U_0 = 4\pi \times 10^{-7}$ H/m, the current of the high voltage line is $I = 1000$ A, the distance between the four wires is L, and the maximum distance between the current carrying coil and the high voltage line is $d_0 = L_{OA} = 0.02$ m. Let K_1 denote the ratio of the combined magnetic induction intensity of the high-voltage wire on the Y-axis direction to the magnetic induction intensity of the high-voltage wire A on the Y-axis. In this case, K_1 can be calculated as follows:

$$\begin{aligned} K_1 &= \frac{B_y}{B_{\mathrm{ay}}} \\ &= \left[1 + \frac{L^2_{\mathrm{OA}}}{L^2_{\mathrm{OB}}} - \frac{L^2_{\mathrm{OA}}}{L^2_{\mathrm{OD}}}\right. \\ &\quad \left. + \left(\frac{L \cdot L_{\mathrm{OA}}}{L^2_{\mathrm{OD}}} + \frac{L \cdot L_{\mathrm{OA}}}{L^2_{\mathrm{OC}}} - \frac{L^2_{\mathrm{OA}} \cdot \cos\beta}{L^2_{\mathrm{OC}}}\right)\frac{1}{\sin\beta}\right] \quad (2) \end{aligned}$$

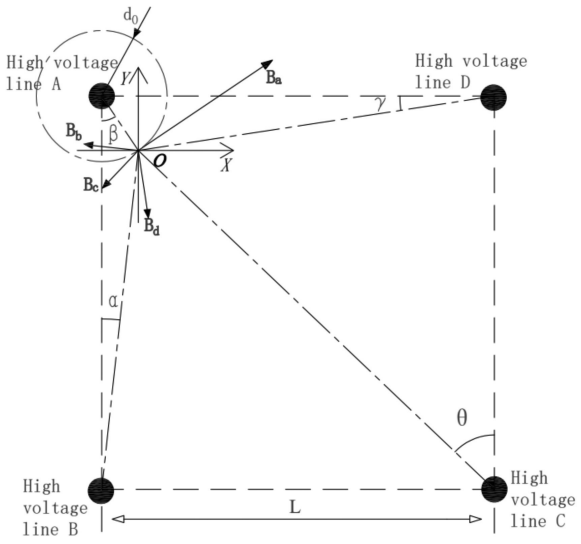

Figure 1. Magnetic field around a four-split wire.

where $L = 0.4$ m, $L_{OB} \in [0.38, 0.42]$, $L_{OC} \in [0.546, 0.566]$, and $L_{OD} \in [0.38, 0.42]$. If these values substitute into (2), K_1 will be approximately 1. Therefore, the combined magnetic field strength of the high-voltage line in the Y-axis is very close in magnitude to the magnetic field strength of high-voltage line A in the Y-axis. Similarly, the combined magnetic field strength of the high voltage line in the X-axis is very close in magnitude to that of the high voltage line A in the X-axis, demonstrating that the generated magnetic fields by high voltage lines B, C, and D have minimal interference with the magnetic fields generated by high voltage line A. Therefore, high-voltage lines B, C, and D are minimally disturbed by the magnetic fields generated by the surrounding high-voltage lines. These findings prove that the magnetic field around the four-split wire is consistent with the theory of a single wire, forming a toroidal magnetic field.

Overhead high-voltage DC transmission lines commonly encounter obstacles, such as vibration dampers, suspension clamps, and jumper wires. Hence, this study conducts magnetic field simulations to analyse the magnetic fields surrounding these three common obstacles. Moreover, their results are compared with the magnetic field simulations around a four-split high-voltage line. Figure 2 illustrates the magnetic field distribution around these three common obstacles and the four-split conductor. The magnetic induction intensities surrounding the three common obstacles and the four-split conductor are $B_a = 5.6 \times 10^{-3}T$, $B_b = 5.2 \times 10^{-3}T$, $B_c = 5.1 \times 10^{-3}T$, and $B_d = 5.3 \times 10^{-3}T$, respectively. The simulation findings confirm that the magnetic field distribution around the high-voltage line in proximity to the three common obstacles aligns with the magnetic field distribution around the four-split conductor, thereby forming an annular magnetic field.

Simulation is used to verify the theoretical analysis. The simulation results prove that the magnetic field around the four-split wire and the wire near the obstacle exhibits a toroidal pattern, which is consistent with the magnetic

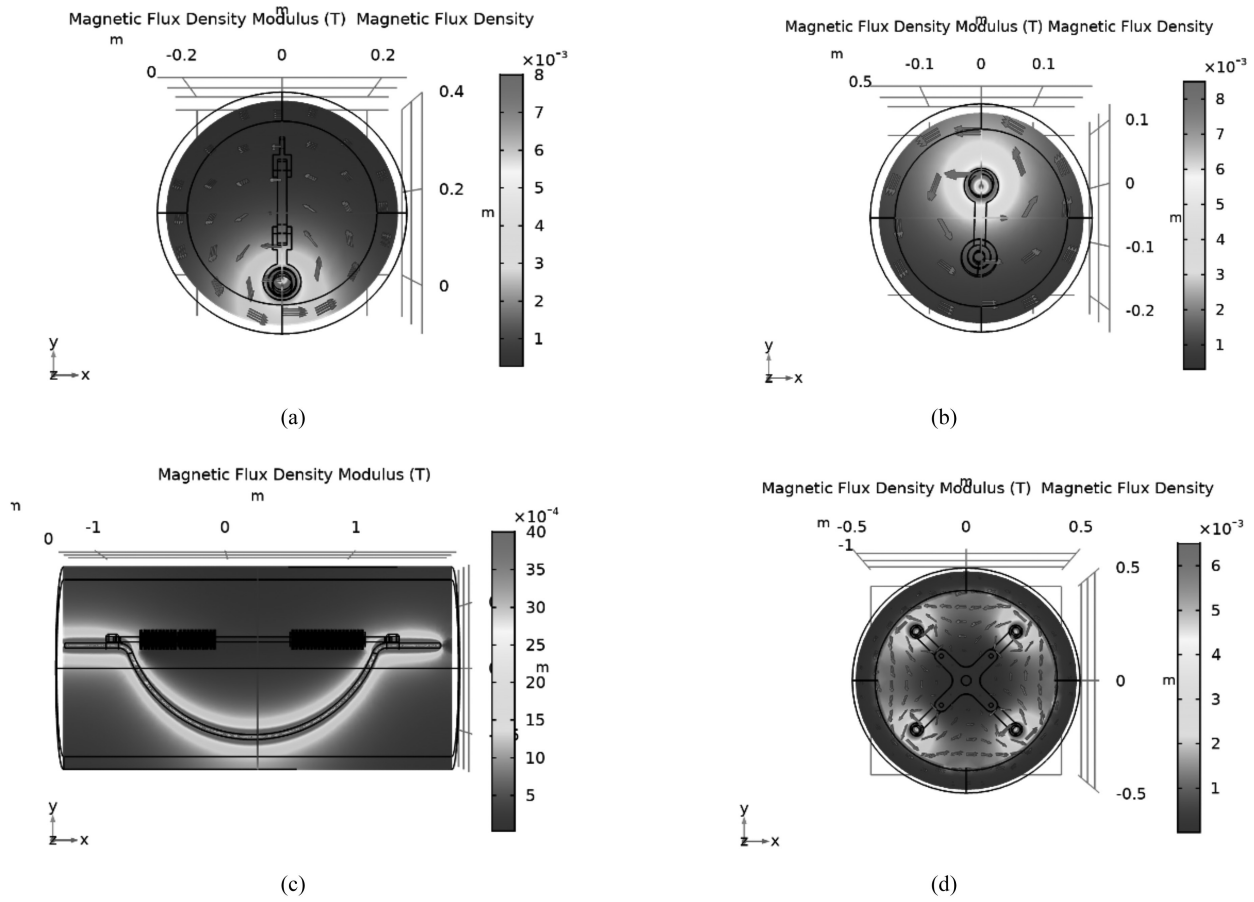

Figure 2. Simulation of the magnetic field around the wire near various obstacles: (a) suspension clip; (b) anti-vibration hammer; (c) jumper; and (d) four-split conductor.

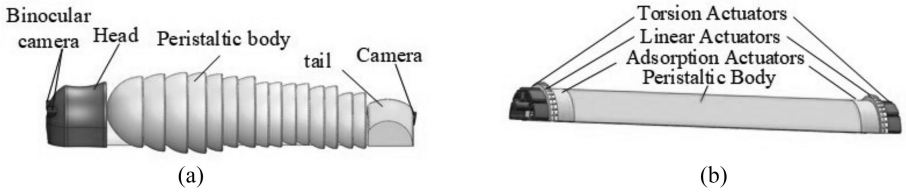

Figure 3. Body configuration: (a) external structure diagram and (b) internal function diagram.

actuation theory based on the magnetic field around the wire is certain (or nearly) necessary in this paper.

2.2 Body Configuration

The overall configuration of the high-voltage magnetostrictive soft robot inspection system is shown in Fig. 3, and its appearance is designed to resemble the shape of a worm. The external structure comprises the head, tail, and crawling body. The head and tail are embedded with motors and sensors (not shown in the figure for simplicity) and equipped with mono and stereo cameras to detect obstacles in the high-voltage line. The internal structure consists of four parts: torsional drivers (2), linear drivers (2), adhesion drivers (2), and the crawling body (1). The magnetic force drivers enable the robot to be driven, rotated, and adhered to the surface, eliminating the need for additional actions, improving inspection efficiency, and reducing the overall size of the robot. The motion states of the high-voltage magnetostrictive soft robot inspection system while crossing obstacles are shown in Fig. 4. The soft robot flexibly traverses suspension clamps and jumpers and crosses insulator discs and shock absorbers by crawling in an "Ω" shape.

3. Obstacle-Surmounting Analysis of Magnetodynamic Soft Robot

3.1 Driving Mechanism of Magnetically Actuated Soft Inspection Robot

According to the ampere force principle, wherein the current-carrying coil receives the annular magnetic field around the high-voltage DC wire as the driving force,

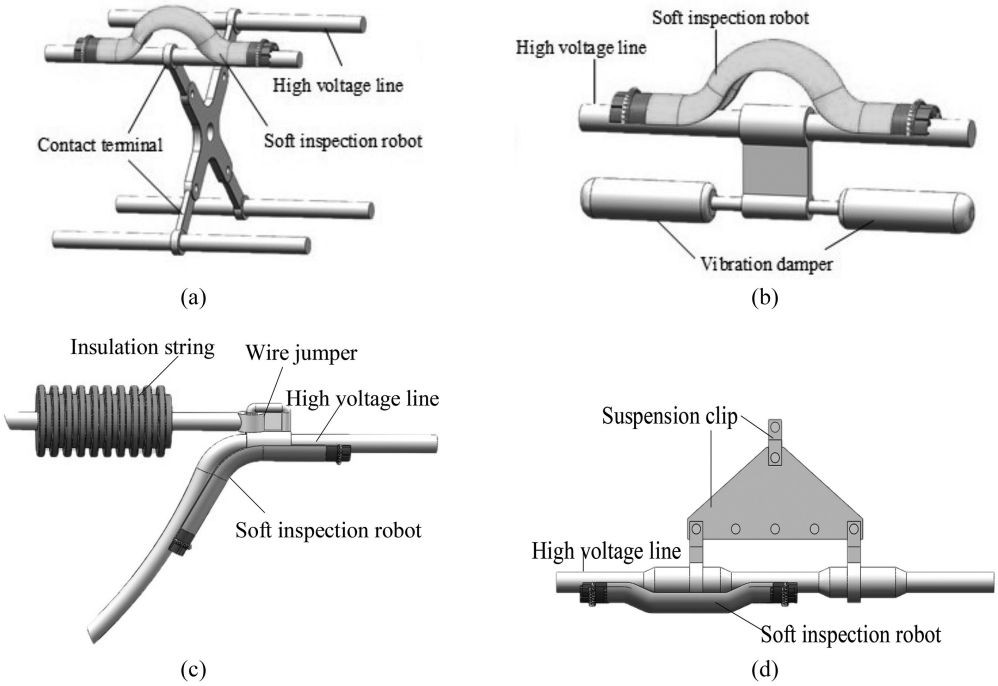

Figure 4. The pose of the soft robot across obstacles: (a) cross clip; (b) cross shock hammer; (c) jumper; and (d) spanning overhang clips.

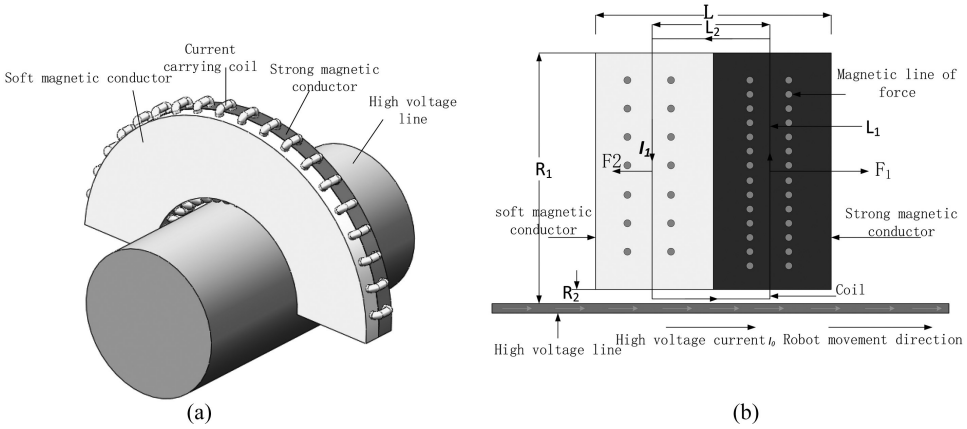

Figure 5. Magnetic linear drive working mechanism: (a) solid model and (b) physical model.

the current-carrying coil is coupled into the soft material to form a driving, adsorbing, twisting magnetic drive, and a creeping body. Moreover, the robot passes through the drive, and the cooperation with the peristaltic body completes a series of obstacle-crossing actions. The soft body of the robot is constructed using polyurethane, while powder core polyurethane is used in the individual actuators and creepers for strong magnetic conductivity. The powder core strengthens the high-voltage DC magnetic field, thereby improving the magnetostatic force of the actuators [16]–[19]. The density of the polyurethane material is denoted as $\rho = 1.1 \sim 1.25$ g/cm^3, and the weight of the magnetically actuated soft robot is less than 2 kg, depending on the robot's dimensions. The magnetic linear drive provides ampere force in the working direction of the robot, as shown in Fig. 5. Using a current-carrying coil to generate an ampere force within a toroidal magnetic field surrounding a high-voltage DC wire. The long side of the current-carrying coil is placed within both the strong magnetic conductor and the soft magnetic conductor, while the short side is placed in the non-magnetic conductive material.

The magnitude of the magnetic field at any point in the magnetic conductor at a distance r from the centre of the wire is:

$$B = u_0 u_r I_0/(2\pi \mathrm{r}) \tag{3}$$

where $u_0 = 4\pi \times 10^{-7}$ indicates the vacuum permeability, u_r represents the relative permeability of a strong magnetic conductor, and I_0 denotes the high voltage DC current. Assuming the current of the current-carrying coil is I_1, the magnitude of the linear driving force of the magnetic force

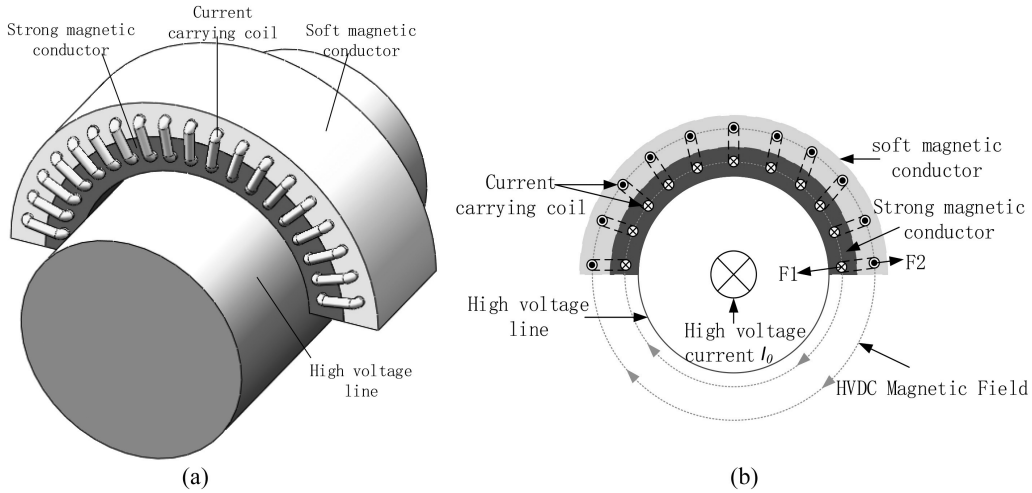

Figure 6. Working mechanism of magnetic adsorption: (a) solid models and (b) physical model.

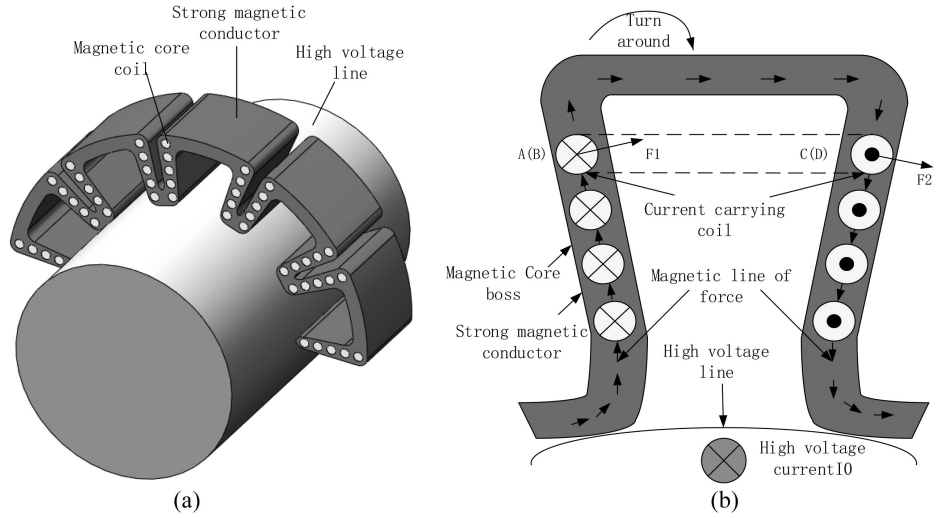

Figure 7. Working mechanism of magnetic torsion: (a) solid models and (b) physical model.

can be calculated as follows:

$$F_1 = \int_{R_2}^{R_1} \frac{u_0 u_r I_0}{2\pi \mathrm{r}} I_1 \mathrm{dr} \tag{4}$$

Given $I_1 = 10$ A, $I_0 = 1000$ A, $R_2 = 0.024$ m, $R_1 = 0.046$ m, $u_0 = 4\pi \times 10^{-7}$, $u_r = 1000$, and the number of turns of the coil of 30, the amperage of a single magnetic linear actuator is $F_{30} = 39$ N. The magnetic soft robot is equipped with magnetic linear drives at the head and tail, enabling the entire robot to receive a linear drive of 78 N.

The magnetic adsorption drive provides the ampere force for the robot to cling steadily to the high-voltage wire, as shown in Fig. 6. The adsorber consists of a strong magnetic conductor in the inner layer and a soft magnetic conductor in the outer layer, with the current-carrying coil embedded in the material. The amperage in the coil is much greater in a strong magnetic conductor compared to the soft magnetic conductor, *i.e.*, $F_1 \gg F_2$. Then, F suction can be obtained as follows:

$$\begin{aligned} F_{\text{Adsorption}} &= BIL = \frac{u_0 u_r I_0}{2\pi \mathrm{r}} I_1 L \\ &= 30 \times \frac{4\pi \times 10^{-7} \times 0.5 \times 10^3 \times 10^3}{2\pi \times 0.05} \\ &\quad \times 10 \times 0.2 = 250N \end{aligned} \tag{5}$$

where $u_r = 500u_0$, $I_1 = 10$ A, $I_0 = 1000$ A, $r = 0.05$ m, $L = 0.2$ m, and the number of turns is 30. When a high-voltage magnetically actuated soft body inspection robot is in motion, at least one adsorption driver must cover the high-voltage line to ensure the robot's safety. In this article, the maximum adsorption force provided by a single magnetic adsorber is 250 N, and the overall weight of the robot is 20 N. The magnetic torsion drive provides the ampere force when the robot is torsion, as shown in Fig. 7. In this configuration, the AB and CD sides of the magnetic core are embedded in the strongly magnetic conductor. Consequently, the AB side is subjected to the ampere force F_1, which acts perpendicular to the radial direction of the

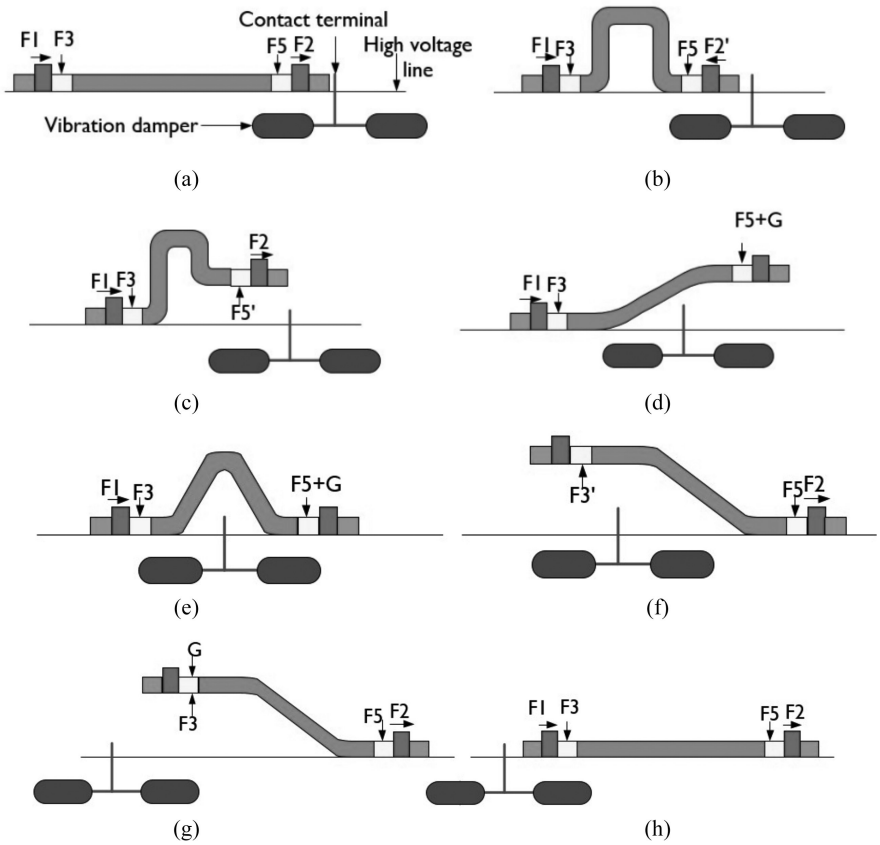

Figure 8. Analysis of the action of the anti-vibration hammer across.

magnetic core. Similarly, the CD side experiences the same ampere force, F_2 and its direction is perpendicular to the radial direction of the magnetic core. Therefore, the coil is subjected to torque, which can be determined as follows:

$$M = F \cdot r = (u_0 u_r I_0 I_1 L \cdot r)/2\pi \mathrm{r} \tag{6}$$

Considering the magnetic coil as 25 turns, the number of effective sides is 50, and the length of the coil is $L =$ 50 mm. Therefore, the torque provided by the magnetic torsional drive can be calculated below.

$$\begin{aligned} M &= 50F \cdot r = 50 \times u_0 u_r I_0 I_1 \mathrm{Lr}/(2\pi \mathrm{r}) \\ &= 50 \times 4\pi \times 10^{-7} \times 10^3 \times 10^3 \times 10 \times 0.05 \div 2\pi \\ &= 5N \cdot m \end{aligned} \tag{7}$$

As the robot has one head and one tail, the maximum torque of the robot is 10 N.m. Even after the robot gains weight, the magnetic torsional adsorber can be cascaded to generate greater torsional torque.

4. Analysis of the Movement Across the Barrier

When the robot performs inspection, it requires crossing the spacer bar, anti-vibration hammer, suspension wire clips, and jumper. Spacer bars and anti-vibration hammers are creeping obstacles (spacer bars are not elaborated as they are crossed the same way as anti-vibration hammers), and the suspension wire clips and jumper are compliant in overcoming obstacles. Conduct an analysis of the obstacle-crossing manoeuvre for the actions described above when encountering obstacles.

As shown in Fig. 8, the high-voltage magnetically actuated soft body inspection robot uses two-ampere forces, F_1 and F_2, generated by a magnetic linear actuator to drive the robot in a linear motion. Moreover, the adsorption actuator generates F_3 and F_5 to stabilise the robot wrapped around the high-voltage line. When the robot moves close to the anti-vibration hammer, it generates F_2' by changing the current direction in the magnetic linear drive close to the anti-vibration hammer. As a result of the combined action of F_1 and F_2', the robot's peristaltic body is squeezed by the flexibility of the peristaltic body, as shown in Fig. 8(b).

Ampere forces, F_5' and F_2, of the adsorption driver and the linear driver close to the obstacle squeeze the magnetic peristaltic body to a sufficient height required for crossing the anti-vibration hammer and preparing the robot for crossing the obstacle, as shown in Fig. 8(c). When the height can be over the height of the obstacle, to balance the robot's gravity, the robot is steadily suspended in mid-air by varying the amount of current in F_5'. In Fig. 8(d), F_5 is generated by changing the direction of the current in the front adsorption driver when crossing an obstacle, causing the robot to fall back to and stabilise on the high voltage line, as shown in Fig. 8(e). Subsequently, by disconnecting the current in F_1 and changing the current direction in F_3, F_3' is generated, allowing the second half of the robot to pass steadily through the obstacle, as

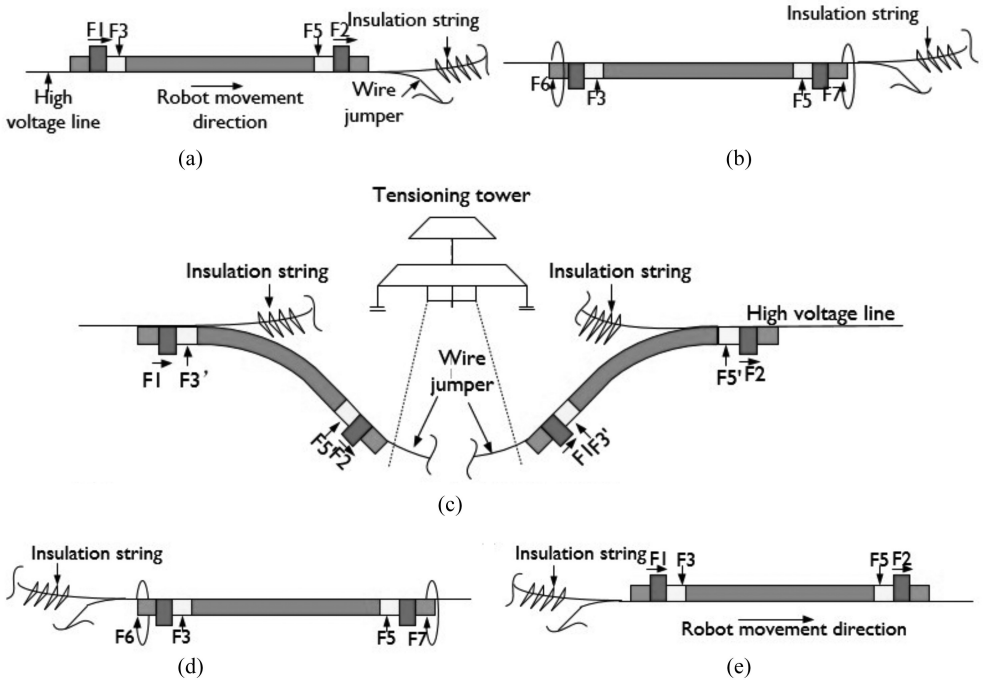

Figure 9. Analysis of the action across the line.

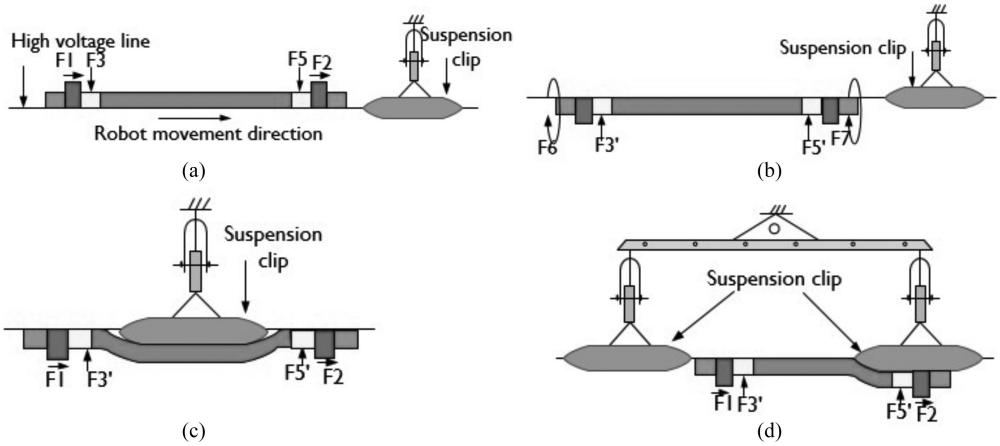

Figure 10. Analysis of the action of crossing the suspension clamp.

presented in Fig. 8(f). When the second half of the robot successfully passes the obstacle, the entire robot is brought back down to the high voltage line by reducing the current in F_3', as shown in Fig. 8(g). Following the completion of the crossing, the robot works steadily on the high-voltage line, using magnetic linear drives and adsorption drives.

As shown in Figs. 9 and 10, the high-voltage magnetically actuated soft body inspection robot straddles the suspension clips and jumpers by compliantly crossing obstacles. Firstly, the driving force generated by the magnetic linear drive and the adsorption force generated by the magnetic adsorption drive enables the robot to operate properly on the high-voltage line. Subsequently, the torsion forces F_6 and F_7 are generated by the magnetic torsion drive rotate the robot 180°. This rotation allows the robot to go over obstacles in the most convenient way. When the robot passes through obstacles, the flexibility of the soft robot is used to cross jumpers and suspension clamps smoothly. Furthermore, F_3' and F_5' are generated by increasing the current of the magnetic adsorber, ensuring that the robot is stably attached to the high-voltage line. After the robot crosses the obstacle, the magnetic twister starts to energise, and the robot is rotated 180° back to a stable working state. At this point, the obstacle-crossing task of the robot is completed.

The forces $F_1, \ldots,$ and F_7 involved in crossing the obstacle are amperometric forces generated by the magnetically actuated actuator. Specifically, F_1 and F_2 are the amperometric force generated by the magnetic linear actuator, with a single theoretical value of 39 N. F_3 and F_5 represent the amperometric force generated by the magnetic adsorption actuator, with a theoretical value of 250 N each. Lastly, F_6 and F_7 denote the amperometric force generated by the magnetic torsion actuator, with a

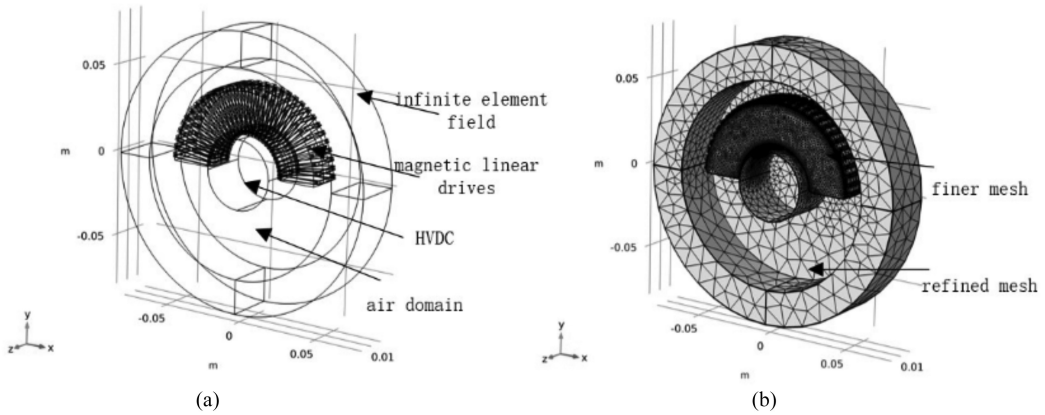

Figure 11. Simulation model of magnetic linear drives: (a) physical model and (b) meshing.

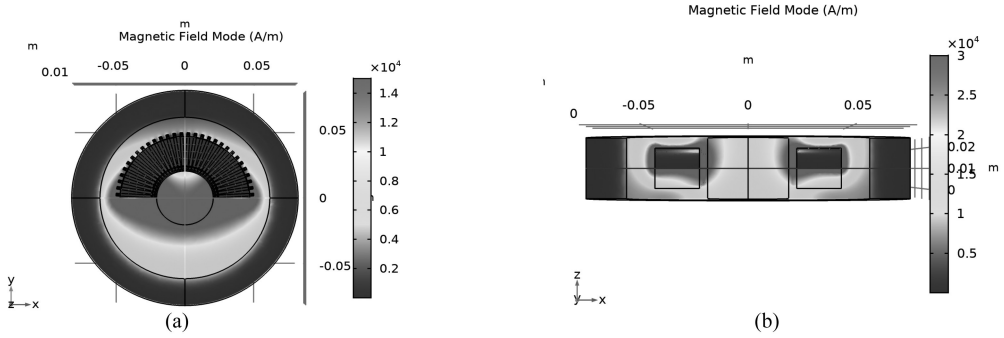

Figure 12. Simulation results of a 30-turn coil for a linear drive: (a) xy and (b) xz.

theoretical value of 10 N.m. The robot's linear drive and torsional drive are both somewhat impacted by friction force and torque when it is in motion. Aluminium is typically utilised for constructing high-voltage lines, while polyurethane is used to construct the robot's shell, which comes into touch with the high-voltage wires. The two have a 0.2 coefficient of friction. When a robot is performing linear drive on high-voltage lines, the adsorption forces F_3 and F_5 created by the adsorption drives and the robot's own gravity constitute the positive pressures on the robot. To properly navigate obstacles, the robot must meet the following requirements:

$$F_f = \mu * (mg + F_3 + F_5) < F_1 + F_2 \tag{8}$$

Then, the maximum value of its adsorption force $F3$ and $F5$ should be 185 N, which is greater than the value of gravity. Simultaneously, while the robot is traversing obstacles, one of its ends needs to be positioned far away from the high-voltage line. The robot has only one end of the magnetic driving force and adsorption force, the maximum value of the attachment force is 175 N. In this context, the maximum adsorption force of the magnetic adsorption coil can reach 250 N. Therefore, while the robot is in operation, it is necessary to adjust the number of coil turns and the current magnitude to control the adsorption force.

Therefore, when the robot is driving on the high-voltage line, the number of coil turns and currents should be controlled to control the absorption power, so that the adsorption force is less than 185 N, and the adsorption force of cross-domain obstacles is less than 175 N. The conditions under which the robot can successfully overcome obstacles during rotational motion are:

$$M_f = F_f \cdot R < M \tag{9}$$

where F_f has a maximum value of 78 N and the high-voltage line has a radius of 0.02 m. Consequently, 1.56 N.m of torque is the maximum. The torsional drivers' maximum torque is 10 N.m, and their frictional torque is much less than the magnetic torque. Force and torque are far less significant than they are in theory.

5. Magnetic Actuation Simulation Analysis

To ensure that the theory is accurate and to get ready for further experiments, the magnetic drives are simulated using the COMSOL simulation software. By designing the structure of the magnetic drives and analysing the rationality of its physical system to obtain a physical model. Get the correct numerical precision by properly meshing the physical model. Since the physical model is relatively regular, the physical model is meshed with free tetrahedral mesh. The magnetic drives adopt a finer grid, and the air domain and infinite element domain adopt a finer grid. Process through the mesh for precise numerical results.

For the magnetic linear actuator, the dimensions are as follows: the radius of the high-voltage line is $r_1 = 0.02$

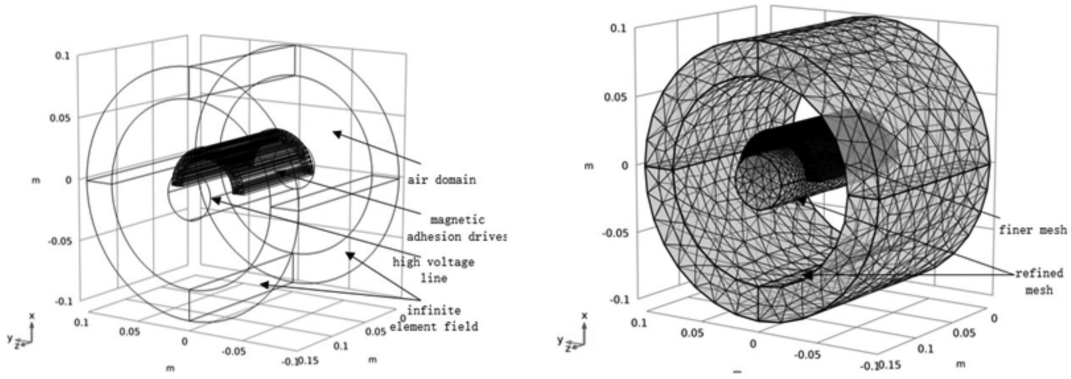

Figure 13. Simulation model of magnetic adsorption drives: (a) physical model and (b) meshing.

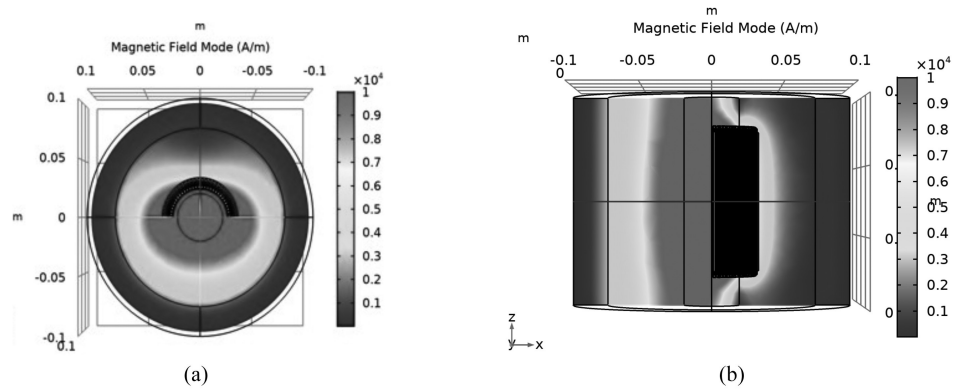

Figure 14. Simulation results of the 30-turn coil of the magnetic adsorber: (a) xy and (b) xz.

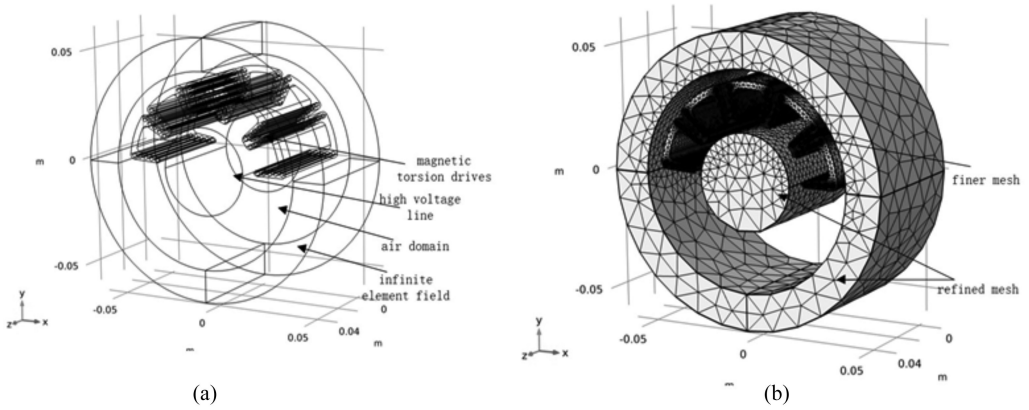

Figure 15. Simulation model of magnetic torsion drives: (a) physical model and (b) meshing.

m, the radius of the air domain is $r_2 = 0.03$ m, and the radius of the infinite element domain is 0.05 m. In addition, the length of the high-voltage line and the air domain is $h_1 = 0.02$ m. Moving on to the magnetic core, its large circle has a radius of $r_b = 0.046$, while this value for the small circle of the magnetic core is $r_s = 0.024$ m. The length of the magnetic core is 0.02 m, and the cross-sectional area of the coil is $(0.001 \times 0.001\pi)$ m^2, with the coil consisting of 30 turns.

The simulation result indicates that the ampere force in the Z-direction is -43.191 N. In comparison, the theoretical value obtained above was $Fz = -39$ N. The deviation between the theoretical values and the simulation results arises from not considering the coupling in the z-axis direction caused by generating ampere forces in the X- and Y-axis directions. However, the error is $|-39-(-43.791)|/|-43.791| = 0.109$. Hence, the error is within control, and the simulation value is greater than the theoretical value, facilitating the linear drive of the robot.

For the magnetic linear adsorber, take the high-voltage wire radius $r_1 = 0.02$ m, the inner diameter of the magnetic

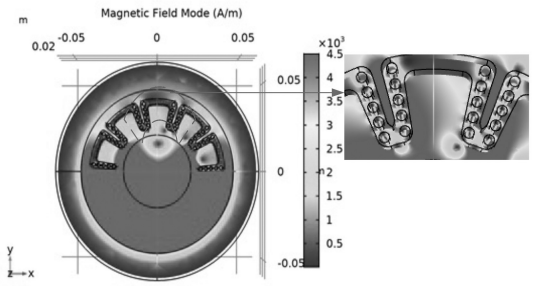

Figure 16. Action results for the 25-turn coil of the magnetic torsion drive.

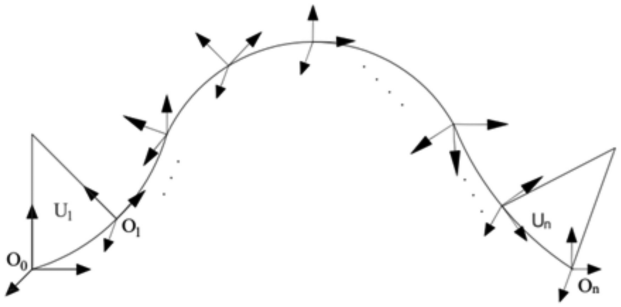

Figure 17. Decomposition of the inspection robot into "Ω" shape.

core $r_0 = 0.024$ m, the outer diameter $r_1 = 0.034$ m, the coil radius of the magnetic core clock $r = 0.002$ m. Moreover, the high-voltage current is $I_g = 1000$ A, and the current-carrying coil is $I_{\text{coil}} = 10$ A.

The ampere force in the X-direction is calculated as 243.40 N. Comparing this with the theoretical value of $F_z = 250$ N, it is evident that the simulated and theoretical values tend to be equal. In this case, the error is $|250 - 243.40|/243.40 = 0.0271$, indicating that the error is within the controllable range.

For the magnetic torsion adsorber, the parameters are set as follows: the high-voltage wire radius is $r_g = 0.02$ m, the inner diameter of the boss coil is $r_1 = 0.024$ m, the outer diameter is $r_2 = 0.04$ m, and the coil radius is $r = 0.002$ m in the magnetic core. In addition, the high-voltage current is $I_g = 1000$ A, and the current-carrying coil is $I_{\text{coil}} = 10$ A.

The axial torque is -4.7 N, and the above theoretical torque is 5.0 N, which is similar to the theoretical value. In this case, the error is $|5.0 - 4.7|/4.7 = 0.063$, which is within the controllable range. The above simulations demonstrate that the minimum ampere force generated by the designed coil is theoretically sufficient to ensure a smooth and efficient crossing of the obstacle by the soft-bodied robot

6. Establishment of Dynamics Model Based on the Lagrangian Dynamics Equation

The analysis of the motion involved in overcoming obstacles indicates that the high-voltage magnetostrictive soft robotic inspection robot exhibits the most complex locomotion when performing "Ω"-shaped crawling over obstacles. Thus, a mathematical model is developed for this motion and the Lagrangian dynamics method is applied for the dynamic modelling [20]. The mathematical model for the "Ω"-shaped obstacle traversal should satisfy the following conditions:

(1) The high-voltage magnetostrictive soft robotic inspection robot forms a continuous.
(2) and smooth curve after bending, with the equal curvature at every point along each segment U_i.
(3) The soft material is defined as incompressible.
(4) The curve represents the morphology of the soft robot, which can be divided into i segments (where $i \in \{1, 2, 3, \ldots, n\}$).

As shown in Fig. 17, the "Ω" curve comprises three curves with the same bending directions but different curvatures. To conduct a comprehensive geometric analysis, a micro-unit U_i of the "Ω" curve is considered, as depicted in Fig. 18(a). The Y-axis is perpendicular to the robot's end face and points outward. The bending angle θ_i is the angle between Y_{i-1} and Y_i, representing the curvature of the soft robotic segment. Additionally, the rotation angle φ_i is defined as the angle between the bending plane of the soft robotic segment and the X-axis. The lengths of the four directions of the soft robotic segment $l = [l_1, l_2, l_3, l_4]$, and their variations $q = [q_1, q_2, q_3, q_4]$, along with the central arc length l_i, are analysed to determine the robot's bending state and motion. Moreover, the radius of the cross-section $\mathrm{X_iZ_i}$ is denoted as R_i, with the X-axis directed from the origin O towards 1, and the Z-axis directed from the origin O towards 4, following the right-hand rule. The relationship between curvature and arc length is given by $\theta_i = l_i \times k_i$, where l_i represents the arc length and k_i indicates the curvature.

The homogeneous transformation matrix of the soft robotic system can be inferred based on the constant curvature segmentation method.

$$
{}^{ij-1}_{\mathrm{ij}}U(K_{\mathrm{ij}}) = \begin{bmatrix} 1 + c^2\varphi(c\theta - 1) & \mathrm{s}\varphi\mathrm{c}\varphi(c\theta - 1) & \mathrm{c}\varphi\mathrm{s}\theta & \frac{\mathrm{c}\varphi(1-c\theta)}{k_{ij}} \\ \mathrm{s}\varphi\mathrm{c}\varphi(c\theta - 1) & c^2\varphi(1 - c\theta) + c\theta & \mathrm{s}\varphi\mathrm{s}\theta & \frac{\mathrm{s}\varphi(1-c\theta)}{k_{\mathrm{ij}}} \\ -c\varphi s\theta & \mathrm{s}\varphi\mathrm{s}\theta & \mathrm{c}\theta & \frac{\mathrm{s}\theta}{k_{\mathrm{ij}}} \\ 0 & 0 & 0 & 1 \end{bmatrix} \tag{10}
$$

The magnetostrictive soft robotic inspection robot's motion state aligns with the working plane. Thus, there exists a rotation matrix of $R_{Y(\varphi)}$ as follows:

$$
R_Y(\varphi) = \begin{bmatrix} \mathrm{c}\varphi & 0 & \mathrm{s}\varphi \\ 0 & 1 & 0 \\ -s\varphi & 0 & \mathrm{c}\varphi \end{bmatrix} \tag{11}
$$

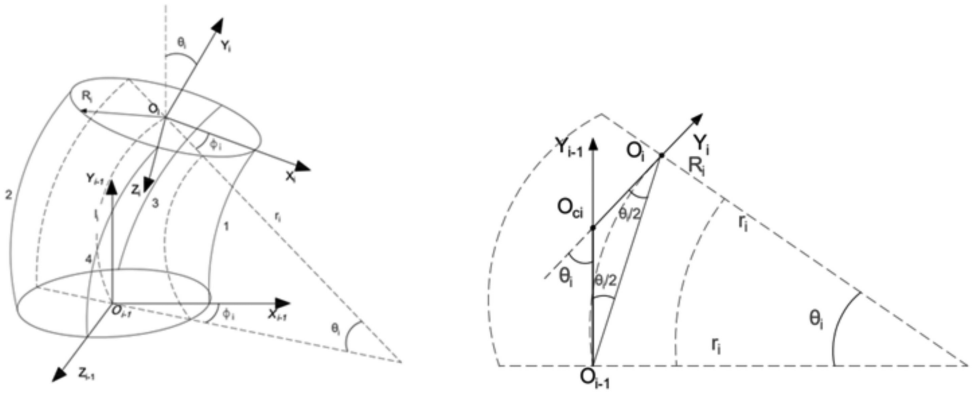

Figure 18. Morphological decomposition of the microcell Ui: (a) decomposition of the kth segment of the Ui morphology and (b) cross-sectional diagram of the kth.

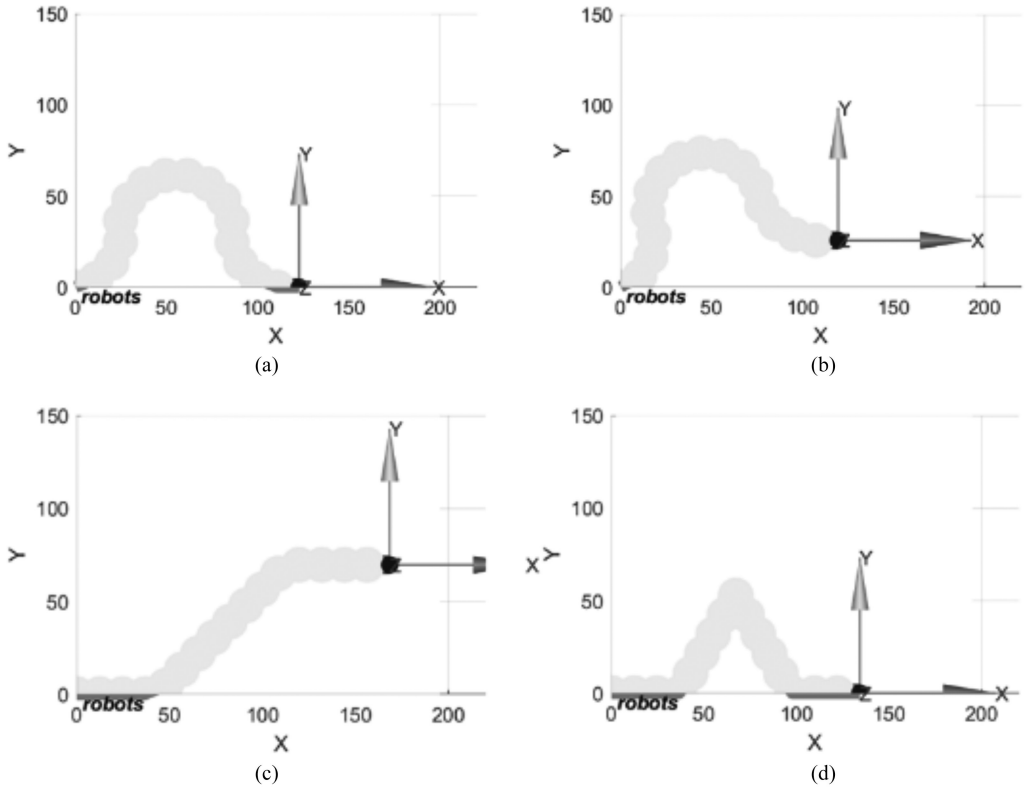

Figure 19. Motion attitude simulation.

The homogeneous transformation matrix of the soft robotic system is as follows:

$$T_{\mathrm{ij}} = {}^{00}_{\mathrm{nm}}\, T(K_{\mathrm{ij}}) = \prod_{i=1}^{n}\prod_{j=1}^{m} {}^{ij-1}_{\mathrm{ij}}\, U(K_{\mathrm{ij}}) = \prod_{i=1}^{n}\prod_{j=1}^{m} \begin{bmatrix} R_Y(\varphi) \cdot {}^{ij-1}_{\mathrm{ij}} & R \\ 0 & 1 \end{bmatrix} \begin{bmatrix} R_Y(\varphi) \cdot {}^{ij-1}_{\mathrm{ij}} & P \\ 0 & 1 \end{bmatrix} \quad (12)$$

Figure 19 presents the performing motion simulation using MATLAB for its homogeneous transformation matrix.

As shown in Fig. 18(b), the centroid of the k_{th} segment is located at O_{ci} with coordinates (x_{ci}, y_{ci}, z_{ci}). Therefore, according to the geometric relationship derived from the profile diagram of the k_{th} segment of micro-unit U_i, the following equation is concluded based on the profile diagram of the k_{th} segment and the decomposition diagram of micro-unit U_i's shape:

$$x_{\mathrm{ci}} = l_i \cos\phi_i f_1 \quad y_{\mathrm{ci}} = l_i \sin\varphi_i f_1 \quad z_{\mathrm{ci}} = l_i f_2 \qquad (13)$$

Where $f_1 = \{(1 + c_2\frac{i}{k})\sin[c_1\ln(1 + c_2\frac{i}{k})] - c_1(1 + c_2\frac{i}{k})\cos[c_1\ln(1 + c_2\frac{i}{k})] + c_1\}/(1 + c_1^2)c_2c_1 = 2\sqrt{(l_3 - l_1)^2 + (l_4 - l_2)^2}/(R_i - R_{i-1})C_2 = (R_i - R_{i-1})/R_{i-1}$

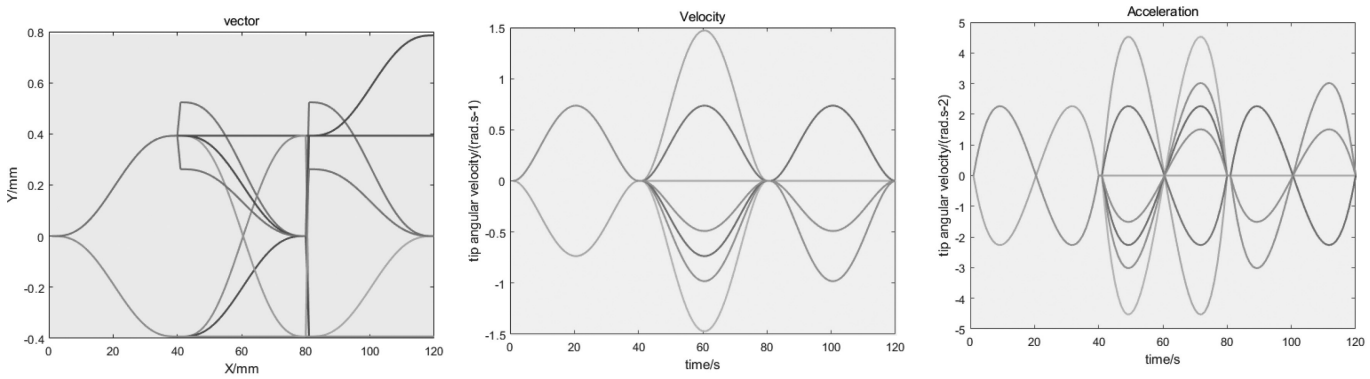

Figure 20. Displacement angular velocity and acceleration simulate.

Differentiating the coordinates of the centroid with respect to time t gives its velocity, denoted as $v_i = (\dot{x}_{\mathrm{ci}}, \dot{y}_{\mathrm{ci}}, \dot{z}_{\mathrm{ci}})$. Given that the density of the soft robot is denoted by ρ and the current length of the central arc is l_i, the mass of the segment is represented as M, which can be expressed as:

$$M = \sum_{k=1}^{n} \rho\pi R_k^2 \frac{l_i}{k} = \rho l_i \pi \left[R_{i-1}^2 + R_{i-1}(R_i - R_{i-1}) + \frac{1}{3}(R_i - R_{i-1})^2 \right] \tag{14}$$

The mass of the U_i segment, denoted as m_i, can be calculated using the following equation.

$$m_i = \rho\pi R_k^2 l/k = \rho l_i \pi [R_{i-1} + (i/k)(R_i - R_{i-1})]^2/k \tag{15}$$

For U_i, the cross-section radius R_k of the disk is much larger than the cross-section height, allowing the rotational moment of inertia J_i rotating around the disk diameter to be expressed as follows:

$$J_i = (1/4) m_i R_k^2 \tag{16}$$

As a result, the angle of rotation β_i is derived from t, and the angular velocity of rotation ω_i in the U_i segment is:

$$\omega_i = \frac{ln[1 + (R_i - R_{i-1})/R_{i-1} * (i/k)]}{2(R_i - R_{i-1})} * \frac{(q_3 - q_1)(\dot{q}_3 - \dot{q}_1) + (q_4 - q_2)(\dot{q}_4 - \dot{q}_2)}{\sqrt{(q_3 - q_1)^2 + (q_4 - q_2)^2}} \tag{17}$$

Then, the kinetic energy of the U_i section includes two parts: the translation of the disk and its rotation. The kinetic energy generated by the disk's translation corresponding to the kinetic energy associated with the disk's centre of mass movement. Thus, the kinetic energy t_i of the U_i section is given by:

$$t_i = \frac{1}{2} m_i v_i^2 + \frac{1}{2} J_i \omega_i^2 \tag{18}$$

Therefore, the total kinetic energy T of the soft robot can be expressed as follows:

$$T = \sum_{i=1}^{n} t_i \tag{19}$$

For a high-voltage magnetically actuated soft body inspection robot, its potential energy includes both gravitational potential energy and elastic potential energy arising from the amperometric force. The total elastic potential energy U_e of the soft-bodied robot results from the cumulative elastic potential energy of its n segments and can be transformed into an integral form as follows:

$$\begin{aligned} U_e &= \sum_{k=1}^{n} u_{\mathrm{ei}} = \sum_{k=1}^{n} \frac{Eq^2\pi R_{i-1}^2}{2L} \left(1 + c_2 \frac{i}{k}\right)^2 \frac{1}{k} \\ &= \frac{Eq^2\pi R_k^2}{2L} \int_0^1 (1 + c_2\delta)^2 \, d\delta \\ &= Eq^2\pi R_k^2 / \left(2L\left(1 + c_2 + \frac{1}{3}c_2^2\right)\right) \end{aligned} \tag{20}$$

Moreover, gravitational potential energy can be determined by the following equation.

$$\begin{aligned} U_g &= \sum_{k=1}^{n} u_{\mathrm{gi}} \\ &= Mg\left(1 + c_2\frac{i}{k}\right)^2 (L - q)\Bigg\{ \left(1 + c_2\frac{i}{k}\right) \left[\cos\left(c_1 \ln\left(1 + c_2\frac{i}{k}\right)\right)\right] \\ &\quad + c_1 \sin\left[c_1 \ln\left(1 + c_2\frac{i}{n}\right)\right] - 1 \Bigg\} \Bigg/ \\ &\quad n\left(1 + c_2\frac{i}{k}\right)(1 + c_1^2)c_2 \end{aligned} \tag{21}$$

The total kinetic energy T and the total potential energy U of the soft-bodied robot are known, and they are substituted into Lagrange's equations to be transformed into universal equations of dynamics:

$$H(q(t))\ddot{q}(t) + \left\{\frac{1}{2}\dot{H}(q(t)) + C(q(t), \dot{q}(t))\right\}\dot{q}(t) + G(q(t)) = \tau(t) \tag{22}$$

The numerical simulation is conducted to analyse the velocity and acceleration of the soft robot, and the results are shown in Fig. 20. The final position of its displacement

is complex and varied. However, its angular velocity and acceleration are kept as smooth curves, proving the relative smoothness of its theoretical motion process.

7. Conclusion

This paper proposed a magnetically actuated soft body inspection robot to address the shortcomings of the rigid multi-cantilever high voltage inspection robots commonly used in domestic and international research, such as large size, bulky body, inflexible barrier crossing, and poor safety. Using the magnetic field force of the annular magnetic field around the high-voltage DC wire to the current-carrying coil to drive the deformation movement of the soft robot, giving full play to the characteristics of the soft robot's redundant degrees of freedom and good flexibility and realising the robot can efficiently and flexibly across various obstacles. Magnetic field analysis and simulation were conducted on four-split high-voltage lines and high-voltage lines around four types of obstacles, proving that the surrounding high-voltage wires generate a toroidal magnetic field to power the robot. Hence, the overall configuration of the soft robot was designed, and posture analysis was performed for the soft robot to cross four obstacles. The minimum driving force required for the soft robot to cross different obstacles was calculated and confirmed to be closely aligned with the theoretical value through simulation, providing evidence of the feasibility of the magnetic actuation scheme of the proposed soft robot. Furthermore, dynamic analysis and modelling were conducted based on the Lagrangian method for the most complex "Ω"-shaped creeping obstacles, demonstrating the feasibility of the theory of soft inspection robots.

References

[1] P. Debenest, M. Guarnieri, K. Takita, E.F. Fukushima, S. Hirose, K. Tamura, and F. Shiga, Expliner-robot for inspection of transmission lines, *Proc. 2008 IEEE International Conf. on Robotics and Automation*, Pasadena, CA, 2008, 3978–3984.

[2] N. Pouliot and S. Montambault, Field-oriented developments for LineScout technology and its deployment on large water crossing transmission lines, *Journal of Field Robotics, 29*(1), 2012, 25–46.

[3] M. Buehler, N. Pouliot, and S. Montambault, Special issue on applied robotics for the power industry, *Journal of Field Robotics, 29*(1), 2012, 1–3.

[4] N. Pouliot, P.L. Richard, and S. Montambault, LineScout technology opens the way to robotic inspection and maintenance of high-voltage power lines, *IEEE Power and Energy Technology Systems Journal, 2*(1), 2015, 1–11.

[5] Z. Weng, T. Liu, C. Wu, and Z. Cao, Mechanism design and kinematic performance research of snake-like robot with orthogonal active wheels, *Proc. Advances in Reconfigurable Mechanisms and Robots II*, Cham, 2016, 603–615.

[6] L. Huang, G. Wu, J. Liu, S. Yang, Q. Cao, W. Ding, and W. Tang, Obstacle distance measurement based on binocular vision for high-voltage transmission lines using a cable inspection robot, *Science Progress, 103*(3), 2020, 0036850420936910.

[7] L. Cheng and G. Wu, Obstacles detection and depth estimation from monocular vision for inspection robot of high voltage transmission line, *Cluster Computing, 22*, 2019, 2611–2627.

[8] J. Del-Cerro, I. Aguirre, and A. Barrientos, Development of a low-cost autonomous minihelicoptor for power line inspections, *Proc. Mobile Robots XV and Telemanipulator and Telepresence Technologies VII*, Boston, MA, 2001 March, 1–7.

[9] S. Montambault, J. Beaudry, K. Toussaint, and N. Pouliot, On the application of VTOL UAVs to the inspection of power utility assets, *Proc. 2010 1st International Conf. on Applied Robotics for the Power Industry*, Montreal, QC, 2010 October, 1–7.

[10] J. D. Hubbard, R. Acevedo, K. M. Edwards, A. T. Alsharhan, Z. Wen, J. Landry, and R.D. Sochol, Fully 3D-printed soft robots with integrated fluidic circuitry, *Science Advances, 7*(29), 2021, eabe5257.

[11] B. McInroe, H. C. Astley, C. Gong, S. M. Kawano, P. E. Schiebel, J. M. Rieser, and D. I. Goldman, Tail use improves performance on soft substrates in models of early vertebrate land locomotors, *Science, 353*(6295), 2016, 154–158.

[12] S. Shian, K. Bertoldi, and D. R. Clarke, Use of aligned fibers to enhance the performance of dielectric elastomer inchworm robots, *Proc. Electroactive Polymer Actuators and Devices (EAPAD)*, San Diego, CA, 2015 April, 417–425.

[13] D.S. Shah, J.P. Powers, L.G. Tilton, S. Kriegman, J. Bongard, and R. Kramer-Bottiglio, A soft robot that adapts to environments through shape change, *Nature Machine Intelligence, 3*(1), 2021, 51–59.

[14] K. Liu, Y. Wu, J. Xu, Y. Wang, Z. Ge, and Y. Lu, Fuzzy sliding mode control of 3-DOF shoulder joint driven by pneumatic muscle actuators, *International Journal of Robotics and Automation, 34*(1), 2019, 38–45.

[15] D. Li, S. Guo, H. Qu, G. Huang, and F. Zhao, Kinematic analysis and optimization of a novel 6-DOF motion simulator mechanism, *International Journal of Robotics and Automation, 32*(6), 2017, 625–638.

[16] K.J. McDonald, L. Kinnicutt, A.M. Moran, and T. Ranzani, Modulation of magnetorheological fluid flow in soft robots using electropermanent magnets, *IEEE Robotics and Automation Letters, 7*(2), 2022, 3914–3921.

[17] G.L. Nor and M.K. Choi, Soft robots based on magnetic actuator, *Journal of the Korean Institute of Electrical and Electronic Material Engineers, 34*(6), 2021, 401–415.

[18] P. Zhang, M. Kamezaki, Z. He, H. Sakamoto, and S. Sugano, EPM–MRE: Electropermanent magnet–magnetorheological elastomer for soft actuation system and its application to robotic grasping, *IEEE Robotics and Automation Letters, 6*(4), 2021, 8181–8188.

[19] C. Yan, X. Zhang, Z. Ji, X. Wang, and F. Zhou, 3D-printed electromagnetic actuator for bionic swimming robot, *Journal of Materials Engineering and Performance, 30*(9), 2021, 6579–6587.

[20] J. Zhang, H. Guo, T. Wang, and J. Hong, The design and motion analysis of a pneumatic omnidirectional soft robot, *International Journal of Robotics and Automation, 32*(6), 2017, 569–576.

Biographies

Xianjin Xu is a Professor with the School of Mechanical Engineering, Hubei University of Technology, Wuhan, Hubei, China.

Haifeng Yan is currently pursuing the master's degree with the School of Mechanical Engineering, Hubei University of Technology, Wuhan, Hubei, China.

Lanlan Liu is a Senior Engineer Hunan Province Key Laboratory of Intelligent Live Working Technology and Equipment(Robot), State Grid of Hunan Electric Power Company, Changsha, China.

Yu Yan is a Senior Engineer with the Hunan Province Key Laboratory of Intelligent Live Working Technology and Equipment(Robot), State Grid of Hunan Electric Power Company, Changsha, China.

YanHao Huang is currently pursuing the Master's degree with the School of Mechanical Engineering, Hubei University of Technology, Wuhan, Hubei, China.

Yuhang Yang is currently pursuing the Master's degree with the School of Mechanical Engineering, Hubei University of Technology, Wuhan, Hubei, China.